nature communications

Article

https://doi.org/10.1038/s41467-026-72831-9

Cure-to-service design of metastability-confined geo-stable cements

Received: 10 September 2025

Accepted: 20 April 2026

Published online: 12 May 2026

Check for updates

Sizhan Liu[1] ✉, Mehmet Topsakal[2], Michael Drakopoulos[3], Jianming Bai[3] ✉, Anastasia G. Ilgen[4] ✉, Toshifumi Sugama[1] & Tatiana Pyatina[1] ✉

Traditional cementitious materials, primarily based on Portland cement, destabilize in hot, corrosive geo-fluids, impeding the advancement of geothermal systems as a scalable energy solution. Yet, identifying geo-stable alternatives that meet multifaceted performance demands throughout the inherently non-equilibrium structural evolution over geothermal well lifetimes remains a fundamental challenge. Here, we present a cure-to-service cement design principle that orchestrates the co-evolution of mechanical properties, phase development and permeability from initial cure through prolonged service, confining metastability by decoupling early-stage Al/Si release to enforce a controlled reaction toward stable aluminosilicate forms. In this design, coarse-grained silica embeds within the nascent boehmite matrix to mitigate permeability, wherein the alkali activator acts as a kinetic lever steering phase selection along the non-equilibrium crystallization pathway. In-situ synchrotron XRD and geochemical modeling show preferential Al dissolution and rapid boehmite formation, while delayed Si availability suppresses premature intermediate formation. Under exposure to supercritical H_2O, analcime serves as a Na^+ reservoir whose gradual dissolution feeds Na-rich phyllosilicates (e.g., paragonite). The nascent composite gains strength and toughness while maintaining low permeability as metastable species convert to stable phases through staged crystallization. This work defines a design principle of aluminosilicate-based cementitious systems for extreme subsurface applications.

As intermittent renewables struggle to meet surging energy demands, the need for baseload, dispatchable power sources has become critical to a resilient, decarbonized future. Among emerging solutions, geothermal systems represent a critical alternative for maintaining energy security, providing a stable output that is independent of weather fluctuations and seasonal variability[1]. Enhanced Geothermal Systems (EGS) extend this potential by engineering subsurface conditions to unlock geothermal resources across diverse locations, addressing renewables' intermittency and supporting the growth in electricity demand driven by emerging technologies such as artificial intelligence, large-scale data centers, national grid optimization, and clean hydrogen production[2]. However, the deployment of EGS faces a critical barrier due to the destabilization of wellbore cement under high temperatures and corrosive brines[3–6], which compromises cement sheath integrity, cement-casing bonding, and long-term zonal isolation.

As cements are emplaced downhole, they undergo solution-mediated phase transformations that drive protracted non-

[1]Interdisciplinary Science Department, Brookhaven National Laboratory, Upton, NY, USA. [2]Nuclear Science & Security Department, Brookhaven National Laboratory, Upton, NY, USA. [3]National Synchrotron Light Source II, Brookhaven National Laboratory, Upton, NY, USA. [4]Geothermal Research Department, Sandia National Laboratories, Albuquerque, NM, USA. ✉e-mail: sizhan1990liu@gmail.com; jmbai@bnl.gov; agilgen@sandia.gov; tpyatina@bnl.gov

Content courtesy of Springer Nature, terms of use apply. Rights reserved

equilibrium crystallization through sequential metastable intermediates over the lifespan of geothermal wells[7–10]. In general, the precipitation of new phases follows Ostwald's rule of stages[11], where phase evolution proceeds through kinetically favored intermediates that nucleate more readily than the equilibrium phases, before gradually recrystallizing into the thermodynamically stable state. Further complicating this process, the temperature ramp prior to reaching the target operational conditions introduces a transient thermodynamic landscape, wherein phases thermally stable at intermediate conditions become unstable as temperature and time evolve. Although the final equilibrium phase remains unchanged, distinct pathways traversing intermediates with varying lifetimes imprint irreversible differences on microstructure and mechanical performance. This complexity underlies the challenge of cementitious materials design for geothermal applications and is driven by the continual reduction of the system's free energy (ΔG) through three coupled factors: (i) the reduction of high internal energy (ΔU) in metastable forms, particularly prevalent in alkali-activated systems[12], such as amorphous gels, poorly bonded hydrates, or reactive interfaces that readily decompose, recrystallize, or dissolve in reactive fluids[13,14]; (ii) entropy-driven processes ($T\Delta S$), including dehydration and dehydroxylation, which increase structural disorder through water release ($\Delta S > 0$) and promote porosity development[15,16]; and (iii) volumetric instabilities ($P\Delta V$) associated with recrystallization and thermal expansion mismatches that initiate microcracking[17]. These intrinsic drivers give rise to multistage crystallization events, initiating from precursors and cascading down the free-energy landscape toward equilibrium phases through a series of metastable-to-stable transformations that reshape chemomechanical behavior throughout the material's service life. In parallel with these intrinsic drivers, extrinsic environmental stressors in geothermal wells, including acidic brines with CO_2-rich fluids, promote carbonation reactions and acid dissolution that modify microstructure and interfacial chemistry. Therefore, achieving long-term mechanical performance requires navigating non-equilibrium crystallization pathways in acid- and CO_2-resistant cement chemistries—either stabilizing long-lived mechanically compatible byproducts or, ideally, designing reaction pathways in favor of targeted equilibrium phases that grant the required mechanical performance. However, the structural complexity in cementitious chemistry, under the dual control of temperature and time, gives rise to a myriad of possible crystallization routes[18–20], often leading to poor phase selectivity and uncontrolled mechanical properties.

Considerable efforts have been devoted to replacing calcium silicate hydrate (CSH) systems, i.e., Portland cement, for high-temperature subsurface applications, given its limited resistance to acid corrosion. In this context, mitigating Ca-related degradation by replacing Ca-silicate chains with charge-balanced aluminosilicates has gained increasing attention. Notably, sodium aluminosilicate hydrate (NASH)-based chemistries, commonly known as amorphous geopolymer systems, have been the most extensively studied and are formed by the simultaneous dissolution of Al and Si under highly alkaline conditions[21,22], yet their utilization under hydrothermal conditions remains an open question[13], which current rationalization strategies broadly address through two categories: (i) reducing metastable phases by transforming them to stable phases or replacing them with thermally inert fillers through supplementary additions[23–27], aggregate modification[28,29], and high-temperature-resistant fiber reinforcement[30–32]; and (ii) extending metastable phase lifetimes by stabilizing hydration products and suppressing dehydration–dehydroxylation through water–binder ratio control[33–35] and microstructure engineering[17,36]. The remaining challenge largely stems from the complex and inevitable low-temperature crystallization in aluminosilicate chemistry, which is inherently difficult to control and highly sensitive to subtle changes in external conditions. A further complication is that variations in raw materials influence Al/Si ratios, which in turn drive distinct crystallization pathways, making it difficult to extend empirical modification strategies across formulations, as they have not been rationalized from general thermodynamic principles. More recently, alternative approaches have explored crystalline composite-based systems, such as our previously reported boehmite (AlOOH)-based cement[37], which demonstrates the potential of leveraging boehmite as the early-stage load-bearing backbone and the long-term aluminum supply in designing crystalline aluminosilicate systems.

In this work, our search for a design enabling phase stability and long-term mechanical reliability was initiated with alkali-activated $Al(OH)_3$ | SiO_2 precursors that, upon geothermal aging, yield phyllosilicates $Na_x[Al_2]^{(oct)}[Si_yAl_{z\text{-}y}]^{(tet)}O_{\frac{5z}{2}}(OH)_{x+y+6\text{-}2z}$ (p-NASH) as in-situ binding structures within the targeted AlOOH|p-NASH|SiO_2 composite. First, AlOOH and p-NASH incorporate structural hydroxyls within strongly bonded lattices, offering superior thermodynamic stability over amorphous or hydrated phases containing non-structural water. Second, the in-situ formation of p-NASH acts as a reactive binding phase that chemically bridges boehmite and silica, thereby progressively enhancing mechanical performance during prolonged geothermal exposure. Third, the disparity in dissolution rates between $Al(OH)_3$ and crystalline SiO_2 under mildly alkaline conditions favors the preferential crystallization of AlOOH in a low-silica aqueous environment, which physically encapsulates silica within the AlOOH matrix and thereby suppresses the premature formation of metastable zeolite phases $Na_xAl_xSi_yO_{2(x+y)}{\cdot}nH_2O$ (z-NASH). As z-NASH phases can transform into more thermodynamically stable NASH forms upon extended thermal exposure, suppressing their formation in the low-temperature metastable regime promotes the direct development of stabilized NASH phases (e.g., p-NASH) at high temperatures. Last, the Al-bearing phases boehmite and p-NASH offer resistance to carbonation and acidic fluids under aggressive geothermal conditions. On the basis of this knowledge, we successfully achieve long-term mechanical stability of the AlOOH|p-NASH|SiO_2 composite under supercritical hydrothermal conditions. In-situ X-ray diffraction reveals the alkali-regulated formation of boehmite during solidification, establishing the initial crystalline backbone. Upon geothermal aging, metastable z-NASH phases act as intermediate sodium reservoirs that temporarily retain Na^+ in solid phases during early-stage reactions, thereby limiting immediate Na^+ loss to geo-fluids. As temperature increases, these phases gradually release Na^+ to facilitate the transformation into thermodynamically stabilized p-NASH, thereby sustaining long-term structural reinforcement through a controlled phase evolution pathway. This study establishes a design strategy that integrates thermodynamic principles with kinetic control, leveraging alkali-guided, temperature- and composition-dependent phase selection in the boehmite–silica system to achieve staged formation of NASH structures. This approach offers a validated route to chemically and mechanically stable cementitious materials capable of long-term performance under geothermal conditions.

Results and discussion

Design principles for geothermal well cements

Designing geothermal well cements requires a strategic shift from end-product-centered paradigms to performance-guided tailoring of intermediate states, as outlined in Fig. 1a. This shift is necessary because geothermal well cements undergo prolonged non-equilibrium reactions in chemically aggressive geo-fluids and remain in a state of progressive phase evolution over extended operational periods. Addressing these challenges requires a redefinition of design priorities. First, the design strategy no longer aims solely for phase stability, but instead strategically manages phase metastability in response to the need to retain mechanical integrity throughout the exposure within the metastable phase regime. Second, controlling the phase transformation in a non-equilibrium process poses significant challenges. Geologically induced temperature gradients complicate the reaction mechanisms, introducing

Content courtesy of Springer Nature, terms of use apply. Rights reserved

https://doi.org/10.1038/s41467-026-72831-9

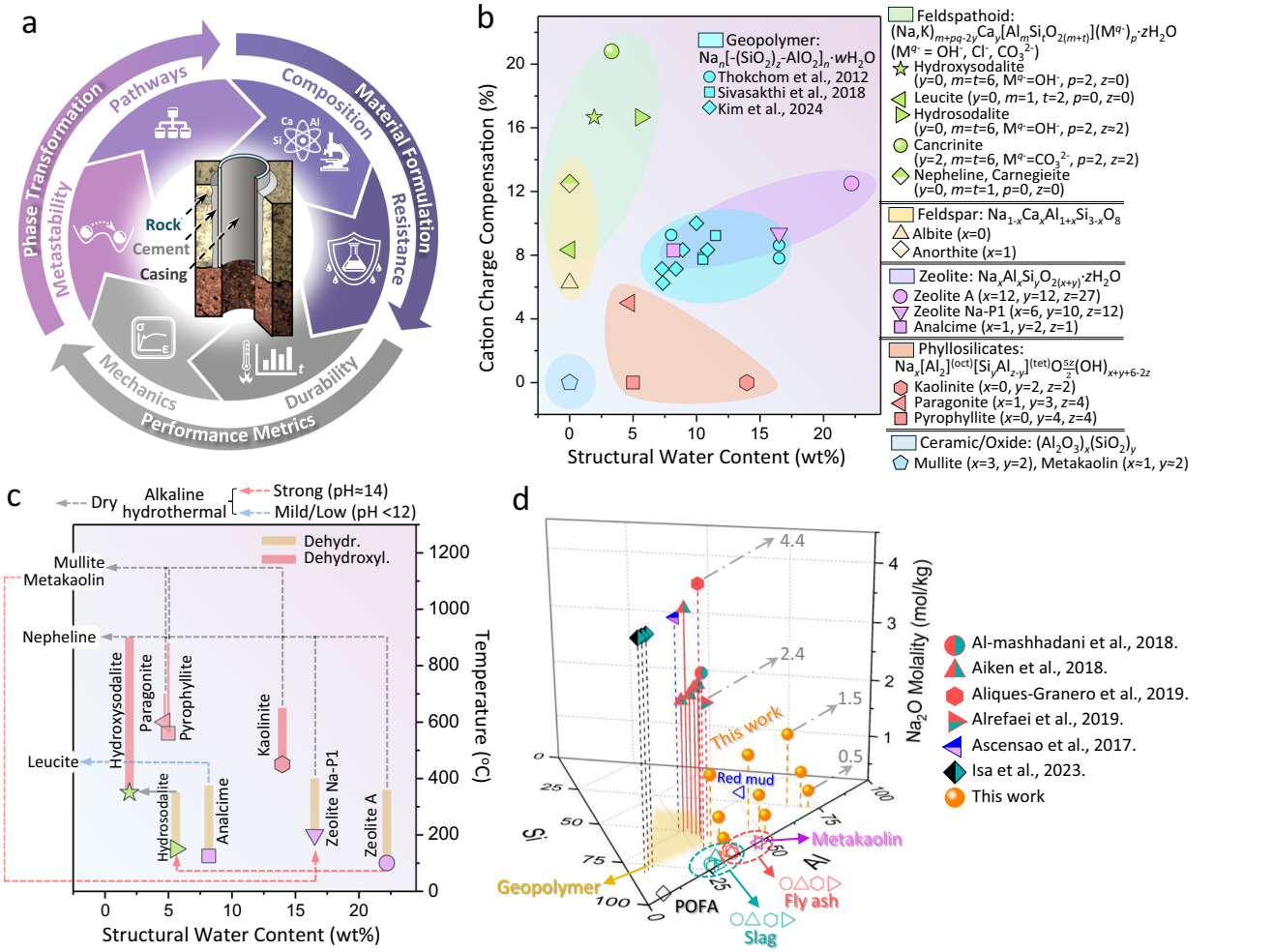


Fig. 1 | Design strategies of cementitious materials for geothermal wells. **a** Schematic illustration of design factors for cementitious systems used in geothermal wells, showing the casing, cement sheath, and surrounding rock. The surrounding segments highlight six design factors: metastability and reaction pathways for phase transformation control; composition and corrosion/carbonation resistance for material formulation; and mechanical performance and durability as key performance metrics. **b** Correlative mapping of structural water content versus cation charge compensation in aluminosilicate families. Structural water content denotes the total H_2O equivalent associated with the structure, including molecular H_2O and equivalent H_2O released by dehydroxylation of structural OH groups. Cation charge compensation denotes the percentage of framework oxygen negative charge balanced by Na, K, and Ca cations. Data points include various crystalline phases (zeolites[38–40], feldspathoids[41–43], feldspar[44,45], phyllosilicates[46–49], ceramic oxides[50]) and geopolymers[51–53]. Shaded fields correspond to distinct structural groups, defined by the level of cation charge compensation required to compensate for framework charge imbalances. **c** Phase evolution of hydrated aluminosilicates under thermochemical conditions. High-alkalinity hydrothermal environments enable interconversion between metastable hydrated phases, whereas anhydrous thermal conditions induce entropy-driven dehydration, forming thermally stable anhydrous phases such as metakaolin or mullite. The reported dehydration and dehydroxylation temperature ranges[54–61] reflect the relative stability of the hydrous components in each phase. **d** Ternary diagram of Na_2O–Al_2O_3–SiO_2 composition (on oxide molar basis), showing raw precursors (hollow symbols) and corresponding activated compositions (filled symbols). Orange symbols represent systems investigated in this study. The vertical axis indicates Na_2O molality (mol/kg water). Gray horizontal arrows mark representative low and high Na_2O molality values reported in the literature for geopolymer synthesis (2.4 and 4.4 mol/kg), as well as the Na_2O molality range used in this work (0.5 to 1.5 mol/kg); these values are not theoretical boundaries but reflect commonly employed conditions in prior studies[62–67]. The plot highlights different types of precursors, including fly ash, slag, metakaolin, palm oil fuel ash (POFA) and red mud, as well as compositional boundaries for geopolymers reported in the referenced studies. Source data are provided as a Source Data file.

potential deviations from the designated reaction pathway. A mechanistic understanding and predictive control of aqueous-mediated mass transport underlying solid-phase evolution is therefore critical to directing mechanical development aligned with design intent. Third, the compositional design space is sharply narrowed by the overlap between the demands of high-temperature stability and economic feasibility. Accessible cementitious chemistries often draw from geologically abundant minerals (e.g., limestone, clay) or industrial by-products (e.g., fly ash, slag), offering economic advantages but limiting compositional flexibility for rational performance tuning. Searching for sustainable feedstocks requires balancing the compositional complexity of precursors with the ability to retain reaction pathway control. Last, corrosion and carbonation resistance must be embedded within all metastable intermediates throughout the reaction pathways because geo-fluid-induced side reactions risk triggering irreversible microstructural defects before the system reaches its designated high-temperature equilibrium phase. In turn, withstanding extreme geothermal exposure demands material systems derived from chemistries persistently stable through staged transformations. This sharply contrasts with final-product-oriented syntheses, which largely overlook the property demands at intermediate stages.

Content courtesy of Springer Nature, terms of use apply. Rights reserved

In practice, nascent hydrate assemblage progressively develops in geo-fluids, where water not only facilitates mass transport but also supports structural metastability through coordination with charge-balancing cations. Accordingly, direct transformation of raw materials into high-temperature, anhydrous crystalline phases is typically hindered. As such, identifying the geo-stable, kinetically stabilized hydrated intermediates with chemically accessible transformation pathways toward thermodynamically favored phase becomes a key criterion for selecting suitable cementitious chemistries. At the level of basic building units (BBUs), the metastable-to-stable phase transformation is rooted in the reconfiguration of BBU geometry, connectivity, and charge properties, directing materials into distinct structural families. With $[SiO_4]^{4-}$ as the prototypical BBU in silicate-based cement systems, substituting Si^{4+} with Al^{3+} introduces negative framework charges that drive charge compensation by hydrated alkali or alkaline-earth cations (e.g., Na^+, K^+, or Ca^{2+}). Such cationic compensation mechanism not only electrostatically stabilizes the framework but also mitigates chemical attack by reducing the permeability of corrosive species through enhanced ionic binding and restricted ion transport channels. Specifically, in sodium-based aluminosilicates, a strong correlation exists between cation charge compensation and structural water content, which emerges as a primary driver of structural family classification, as shown in Fig. 1b. Notably, zeolites[38–40], feldspathoids[41–43], feldspar[44,45], phyllosilicates[46–49], ceramic oxides[50] and geopolymers[51–53] occupy distinct regions of the map, each exhibiting characteristic hydration levels and charge compensation requirements that underpin their structural distinctions. On the other hand, certain hydrated phases are reported to be convertible via hydrothermal processing[54–56], whereas transitions to anhydrous forms typically proceed through solid-state dehydration or dehydroxylation[40,57–60], marked by a temperature range that reflects the relative thermal stability of the hydrous components (Fig. 1c). Particularly, crystalline water exhibits lower thermal stability than hydroxyl groups, reflecting distinct lifetimes that necessitate careful selection of intermediate hydration states in material design. The highly hydrated structures may reconstruct into alternative hydrated phases in aqueous media (e.g., zeolite A → hydrosodalite)[55], whereas in the absence of water, entropy-driven dehydration leads to framework collapse, often accompanied by structural amorphization[61]. To quantify the crystallographic volume contrast associated with such phase transformations, we constructed a cross-family comparison of density and normalized molar volume per Al/Si polyhedron for representative Na-aluminosilicate minerals (Tables S2–S3). As summarized in Fig. S1, zeolitic frameworks exhibit the largest molar volume per Al/Si polyhedron (i.e., the most open polyhedral packing), followed by feldspathoids, feldspars, phyllosilicates, and ceramic oxides, as bulk density progressively increases. Accordingly, reactions from zeolite-like open frameworks toward these denser products can impose comparatively large volumetric contrasts that are typically manifested in microstructural changes, i.e., porosity evolution and/or microcracking development at meso- and micro-scales.

Even though such thermally induced reactions, reflecting metastable-to-stable phase transformation pathways, have been identified under laboratory conditions (i.e., mass-conserved closed systems), they cannot be relied upon in chemically aggressive, semi-open geological environments, where dissolution–precipitation reactions are hindered from proceeding in a controlled manner. As such, rather than attempting to regulate the inherently uncontrollable pathways that dominate the low-temperature metastable phase regime, it is more effective to proactively suppress their formation before the system reaches the designated geological temperature. This strategy relies on moderate alkali activation of carefully selected precursors, whose Al and Si release exhibits distinct kinetic behaviors at low temperatures. Such kinetic decoupling limits the simultaneous availability of both elements during the metastable regime, while still enabling the formation of stable high-temperature aluminosilicate phases under prolonged thermal exposure. This contrasts sharply with geopolymer systems, which typically rely on high alkalinity and highly reactive amorphous raw materials (e.g., slag, fly ash, metakaolin, red mud, palm oil fuel ash (POFA)) to achieve complete dissolution of both Al and Si at low temperatures[62–67], as illustrated in the ternary Si–Al–Na compositional diagram (Fig. 1d, Table S1). Although high alkalinity enables setting and hardening at ambient temperatures, the resulting disordered frameworks may face stability challenges during subsequent thermal exposure[13]. Thus, to avoid the formation of materials dominated by undesirable metastable phases, controlling the timing of component availability becomes essential, for example, by delaying the release of Si through control of its source reactive surface area. In other words, using kinetic restraint to mitigate kinetically driven phase metastability. This kinetic restriction to Si dissolution can be lifted as temperature increases, thereby unlocking its participation in the reaction that enables a direct transition toward stable aluminosilicate forms. This approach offers a streamlined strategy to bypass uncontrolled metastable intermediates, thereby suppressing dehydration, volumetric change, and other thermochemical events that potentially undermine mechanical properties during metastable-to-stable phase evolution under geothermal exposure.

In pursuit of a formulation that meets critical design criteria, we identify a cementitious composite comprising gibbsite ($Al(OH)_3$) powder and coarse-grained crystalline silica (SiO_2), with Na_2SiO_3 serving as a key lever for regulating solution alkalinity. First, $Al(OH)_3$ has been proven to exhibit tunable dissolution kinetics under alkaline conditions[37], enabling the formation of boehmite (AlOOH) through a dissolution–precipitation process, which in turn promotes continued Al dissolution. This behavior supports early-stage mechanical development while imposing kinetic restraint on aqueous Al ions through the competitive interplay between dissolution and precipitation over the temperature ramp. Second, coarse-grained SiO_2 crystallite exhibits limited reactivity during early-stage curing, confining its participation in phase formation to higher temperature regimes and thereby suppressing the formation of metastable z-NASH. Last, upon extended exposure at high geological temperatures, the reaction becomes thermodynamically controlled rather than kinetically governed, leading to the formation of stable binding phases (e.g., p-NASH)[20,68,69] that reinforce mechanical performance in alignment with long-term geothermal stability.

Design tradeoff in geothermal cements

Material design inherently involves tradeoffs[70–73]— mechanical properties must be balanced against a host of functional requirements for formulating cementitious materials. Formulating geothermal well cements involves multiple, often competing design criteria, including mechanical performance, permeability control, chemical durability, setting controllability, and practical considerations such as cost and environmental footprint. Achieving an optimal balance among these parameters remains a central challenge in well cement design. Our previous work demonstrated that a boehmite-based cementitious system offers early-stage strength, chemical stability, and fast setting[37]. Still, achieving sufficiently low permeability at low cost remains in demand for practical applications, as suppressing fluid transport through porosity control effectively minimizes acid-induced degradation. In this work, coarse-grained crystalline silica was introduced to steer phase selection by kinetically suppressing metastable intermediates, while also transiently acting as an inert-like filler that is expected to reduce overall permeability during boehmite matrix formation. However, this dual-function design introduces tradeoffs in mechanical performance, as the coarse particles may adversely affect structural integrity. To address this, we performed a broad compositional screening to assess the influence of initial $Al(OH)_3/SiO_2$ ratios (wt%, 80/20, 60/40, 40/60) and Na_2SiO_3 content (3–9 wt% relative to

Content courtesy of Springer Nature, terms of use apply. Rights reserved

https://doi.org/10.1038/s41467-026-72831-9

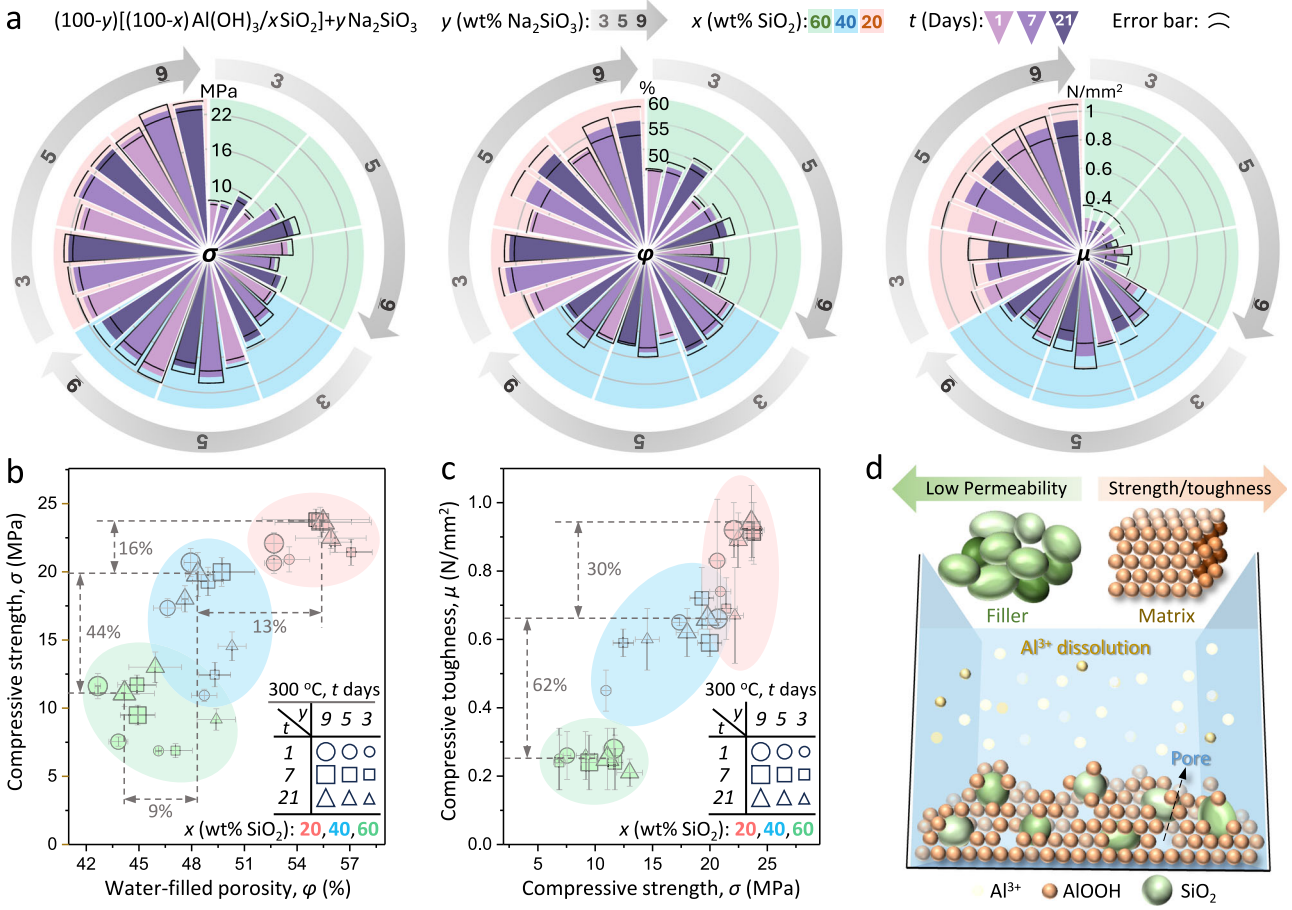


Fig. 2 | Compositional tuning of strength–permeability tradeoff. a Radar plots of compressive strength (σ), water-fillable porosity (φ), and compressive toughness (μ) for alkali-activated aluminosilicate composites synthesized from $Al(OH)_3$, SiO_2, and Na_2SiO_3, with varying silica content (x = 20, 40, 60 wt%) and activator content (y = 3, 5, 9 wt%). Mechanical properties are shown at t = 1, 7, and 21 days of hydrothermal curing at 300 °C. **b** Correlation between compressive strength and porosity. Shaded regions denote different SiO_2 contents. Dashed lines highlight the nonlinear tradeoff between strength and porosity, where increasing SiO_2 from 40 to 60 wt% causes a larger strength loss but only a marginal porosity reduction. **c** Nonlinear response in the toughness–strength relationship. A marked drop in toughness is observed as SiO_2 content increases from 40 to 60 wt%. **d** Schematic illustration of composite formation. Alkali activation via Na_2SiO_3 promotes gibbsite dissolution, leading to a dissolution–precipitation process that generates a dense boehmite-rich matrix. The added SiO_2 particles are embedded within the matrix, which limits pore connectivity and reduces overall permeability. Error bars in **a**–**c** represent standard deviation from three independent measurements per formulation. Source data are provided as a Source Data file.

total solids) on mechanical performance and porosity after hydrothermal exposure at 300 °C for 1, 7, and 21 days. The samples were held at 200 °C for 1 day before the 300 °C treatment. In Fig. 2a, the radar plots show that compressive strength (σ), porosity (φ), and toughness (μ) are strongly influenced by the $Al(OH)_3/SiO_2$ ratio, with increasing SiO_2 content leading to declines in mechanical performance. By contrast, variations due to curing time and activator content are moderate within the 21-day observation window, suggesting that early strength development is primarily from the transformation of $Al(OH)_3$ into AlOOH.

To explore the tradeoffs between strength, porosity, and toughness arising from compositional tuning, Fig. 2b, c visualizes their coupled dependencies within the screened formulation space, enabling identification of statistical trends despite individual error margins. Taking the 21-day samples with 9 wt% Na_2SiO_3 as an example, increasing SiO_2 from 20 to 40 wt% results in a 13 ± 5% reduction in porosity with a 16 ± 9% decrease in strength. However, a further increase to 60 wt% SiO_2 yields just an additional 9 ± 4% drop in porosity, while compressive strength declines sharply by 44 ± 12%. A similar nonlinear trend is observed in the toughness–strength relationship (Fig. 2c). As SiO_2 content increases from 40 to 60 wt%, compressive toughness drops by over 62 ± 24%. In contrast, increasing SiO_2 from 20 to 40 wt% results in a 30 ± 13% reduction in toughness. The uncertainties in the comparative metrics are calculated using standard error propagation, based on measurement errors within typical experimental ranges. Such disproportionate impact of SiO_2 content on porosity and mechanical properties reflects two distinct failure mechanisms associated with silica addition. First, under low-alkalinity conditions, coarse SiO_2 remains largely unreacted and poorly bonded to the surrounding boehmite matrix, thereby weakening local load transfer at grain contacts. Second, as SiO_2 content increases, the accumulation of coarse particles disrupts matrix continuity and undermines percolation pathways for stress redistribution. The decline in mechanical properties at moderate silica addition (i.e., 20 → 40 wt%) corresponds to the former mechanism, whereas the steep drop at 60 wt % SiO_2 arises from the combined effects of both mechanisms, manifested as a pronounced deviation from linear tradeoff behavior. Conversely, as illustrated in Fig. 2d, incorporating SiO_2 disrupts pore connectivity within the matrix, thereby enhancing impermeability—a critical design criterion for cements in geothermal well applications. The observed nonlinear tradeoff reveals a tunable compositional window where permeability can be suppressed without yet triggering matrix failure. Over prolonged hydrothermal exposure, interfacial bonding is expected to improve through the formation of aluminosilicate binding phases, progressively alleviating the tradeoff between mechanical

Content courtesy of Springer Nature, terms of use apply. Rights reserved

https://doi.org/10.1038/s41467-026-72831-9

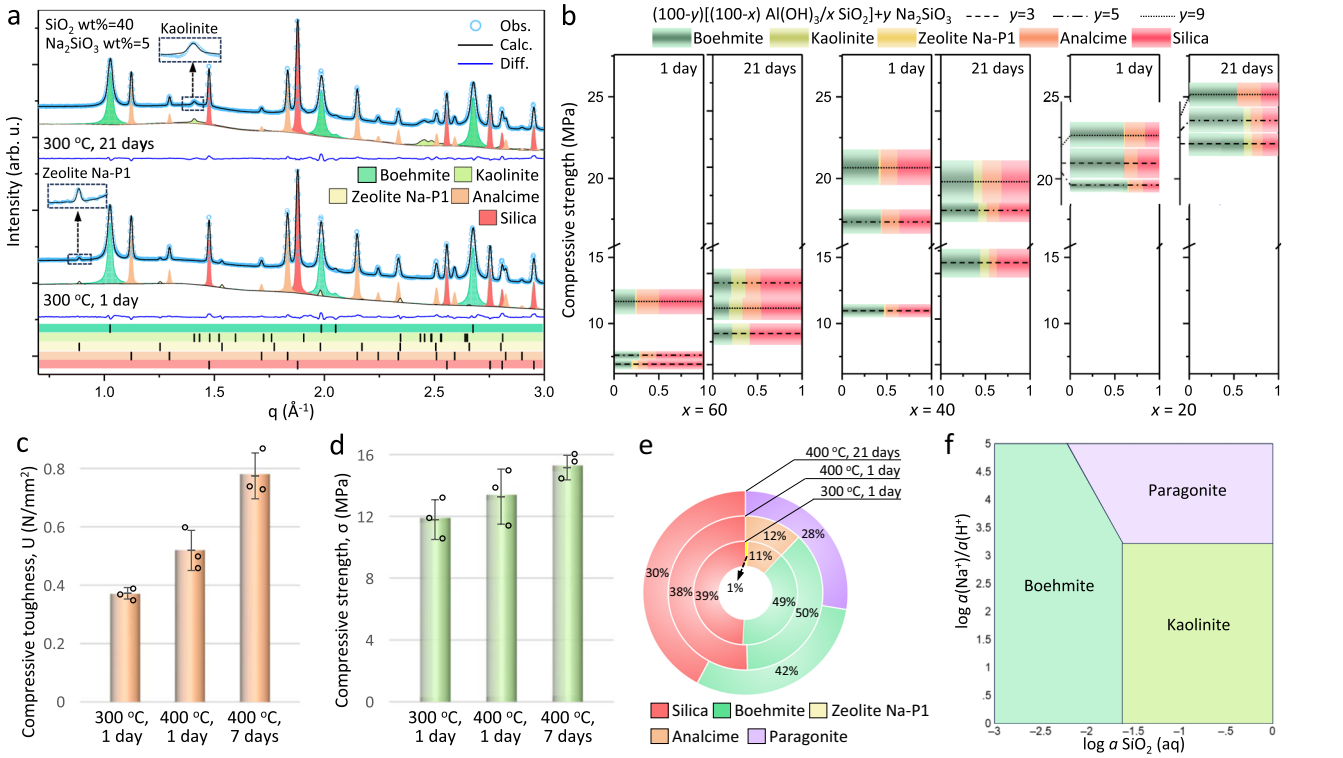


Fig. 3 | Phase evolution of alkali-activated aluminosilicate composites under subcritical and supercritical hydrothermal conditions. a XRD patterns of a representative composite synthesized with 40 wt% SiO_2 and 5 wt% Na_2SiO_3, after sequential exposure at 200 °C for 24 h followed by 300 °C for 1 or 21 days. Insets show the evolution from initially formed zeolite Na-P1 (1 day) to kaolinite (21 days). **b** Summary of Rietveld refinement results for composites synthesized from $Al(OH)_3$, SiO_2, and Na_2SiO_3, with varied SiO_2 (x = 20, 40, 60 wt%) and Na_2SiO_3 (y = 3, 5, 9 wt%) contents. All samples underwent the same exposure protocol as in (**a**). Color bar width indicates standard deviation of compressive strength. **c** Compressive toughness and **d** compressive strength of a formulation with 40 wt% SiO_2 and 5 wt% Na_2SiO_3 directly exposed to 300 °C or 400 °C for 1 or 7 days, to simulate geothermal cementing conditions without prior low-temperature exposure. Error bars represent standard deviation from three independent measurements per formulation. **e** Corresponding phase evolution of samples in **c**, **d**, showing the formation of paragonite after prolonged exposure at 400 °C. **f** Thermodynamic stability diagram showing the predicted domains of boehmite, kaolinite, and paragonite as a function of aqueous silica activity (log $a(SiO_2)$) and sodium-to-proton activity ratio (log $a(Na^+)/a(H^+)$). Paragonite is favored to form at high Na^+/H^+ activity ratios. Source data are provided as a Source Data file.

properties and permeability. SEM-EDX imaging reveals that boehmite remains stably precipitated on silica surfaces after 21-day exposure at 300°C, with Na-rich and Na-deficient aluminosilicate phases surrounding embedded SiO_2 particles (Fig. S2). This motivates further analysis of the underlying phase evolution over exposure time.

Phase evolution under extended geothermal exposure

The relationship between phase evolution and mechanical performance over time provides insight into whether SiO_2, which exhibits low reactivity under mildly alkaline conditions, gradually participates in the development of mechanically reinforcing phases during prolonged geothermal exposure. Therefore, we systematically tracked phase and strength evolution at both subcritical (300 °C) and supercritical (400 °C) temperatures across a series of formulations (Fig. 3). As shown in Fig. 3a, b, Rietveld refinement of the same set of composites analyzed for mechanical performance in Fig. 2 was conducted to investigate phase evolution under prolonged geothermal exposure and its correlation with strength development. The 1-day exposure at 200 °C enabled detection of intermediate phases formed prior to the designated 300 °C treatment. Figure 3a shows the Rietveld refinement result of a representative composite formulated with 40 wt% SiO_2 and 5 wt% Na_2SiO_3. Detailed phase compositions are summarized in Tables S4–S6, and corresponding Rietveld refinement patterns are shown in Figs. S3–S11. After 1 day at 300 °C, trace amounts of zeolite Na-P1 and a comparatively higher fraction of analcime are observed. Over a 21-day exposure, zeolite Na-P1 disappears and kaolinite emerges, whereas analcime remains largely preserved. This transformation suggests that SiO_2, serving as a Si reservoir, is gradually activated at high temperature to release Si into the system. However, Na^+ remains sequestered within residual analcime, thereby favoring the formation of Na-free phyllosilicates, kaolinite. As shown in Fig. 3b, at moderate activator levels (3 and 5 wt%), the observed phase evolution aligns with enhanced compressive strength, suggesting that the formed kaolinite phases contribute to mechanical reinforcement. In contrast, 9 wt% activator addition results in marginal strength gains or even degradation. This is attributed to excess alkali-induced destabilization of the boehmite matrix, as evidenced by the tomographic microstructure comparison given in Fig. S12 and reported boehmite degradation under high alkaline conditions[37].

Moreover, to simulate high-temperature fast curing conditions, the 40 wt% SiO_2, 5 wt% Na_2SiO_3 formulation was selected to be exposed to 300 °C and supercritical 400 °C for 1 and 7 days without 200 °C thermal treatment. As shown in Fig. 3c, d, the resulting compressive strength and toughness increase with extended hydrothermal exposure. Figure 3e further reveals that phase transformation accompanies the development of mechanical strength over time. Notably, under supercritical conditions at 400 °C, the disappearance of analcime is accompanied by the formation of appreciable paragonite, reflecting a thermodynamically controlled reaction pathway. As evidenced by Fig. 3f, the phase stability diagram illustrates that paragonite is favored at high log($a(Na^+)/a(H^+)$) activity ratios, whereas kaolinite dominates under conditions of low Na^+ activity. We propose that at 300 °C, Na^+ remains kinetically trapped within metastable or intermediate phases such as analcime, limiting its participation in

Content courtesy of Springer Nature, terms of use apply. Rights reserved

phyllosilicate formation. At 400 °C, however, these intermediates decompose and release Na^+, enabling the crystallization of thermodynamically stable Na–phyllosilicates. This exposure-activated pathway illustrates how structural evolution under geothermal conditions shapes long-term mechanical behavior.

Design of staged phase formation

Hydrothermal reaction is inherently complex, involving mass transport in aqueous solution and usually proceeding far from equilibrium, governed by the interplay of dissolution kinetics and thermodynamic stability. Elucidating the dissolution kinetics coupled with the structural evolution of cementitious phases is critical for understanding mechanical property development, especially in the early curing stage. To resolve these coupled effects, we performed in-situ synchrotron-based X-ray diffraction, complemented with geochemical modeling, to quantitatively monitor phase evolution and reaction kinetics during exposure, enabling a mechanistic understanding of the multistage crystallization process under relevant alkaline and hydrothermal conditions.

The reactions of cementitious materials proceed through a sequence of stages defined by distinct kinetic and thermodynamic conditions under prolonged hydrothermal exposures. From the perspective of phase formation, the crystallization pathway in cementitious materials can be divided into three stages: an early solidification stage dominated by dissolution kinetics with short-lived metastable species present (stage 1), an intermediate stage where long-lived metastable phases persist (stage 2), and a final stage defined by thermodynamically stabilized end-products (stage 3). Stage 1 is captured by in-situ XRD contour plots in Fig. 4a, b, with Rietveld-refinement-derived quantitative phase analysis given in Fig. 4c, revealing the dissolution of gibbsite, formation of boehmite, and limited reaction of silica during the temperature ramp-up to 300 °C. Details of quantitative refinement analysis are provided in Figs. S13–S19. The emergence and sharpening of the boehmite (020) reflection between 220 and 300 °C provides a direct crystallographic marker for the gibbsite-to-boehmite transformation. The reduction in crystalline phase content in Fig. 4c primarily reflects gibbsite dissolution, with the lost Al species present as dissolved Al^{3+} in the aqueous phase or incorporated into amorphous aluminosilicate gels. The relative fraction changes of gibbsite and non-crystalline phase indicate accelerated Al dissolution at higher activator levels, with the short-lived hydrosodalite phase forming at 9 wt% of Na_2SiO_3 activator. The gibbsite-to-boehmite reaction mechanism and the hydrosodalite formed under excess activator conditions have been studied in our previous work[37].

To further elucidate the mechanistic role of each component during multistage phase transformation, we employed geochemical modeling to uncover the underlying phase selection mechanisms and to rationalize material design through the interplay of thermodynamic stability, kinetic control, and compositional inputs. In Fig. 4d, a geochemical model of a representative system (40 wt% SiO_2, 5 wt% activator) at stage 1 highlights the contrasting dissolution behavior of gibbsite and coarse-grained crystalline silica under mildly alkaline conditions. The modeling reveals that Al^{3+} released from gibbsite dissolution primarily forms boehmite and partially reacts with alkali-derived Si to form hydrosodalite, which exhibits a strong dependence on activator addition, as evidenced in Fig. 4c, where its precipitation is detected only at 9 wt% activator content. Owing to the disparity in dissolution kinetics between gibbsite and silica, the delayed release of silica-derived Si suppresses premature formation of additional aluminosilicate intermediates during stage 1.

The complete precipitation of dissolved Al^{3+} marks the end of stage 1 and initiates the thermodynamically guided progression from stage 2 to stage 3. Clarifying the role of intermediate phases in steering the metastable-to-stable phase transformation (stage 2→ stage 3) provides mechanistic insights into the evolving interplay of phase development, mechanical performance, and microstructure for future studies. As shown in Fig. 4e, the alkali activator not only regulates Al^{3+} dissolution during stage 1, but also, as the initial Na^+ source and pH regulator, dictates the selection of Na-bearing (paragonite) versus Na-free (kaolinite) phyllosilicates during subsequent high-temperature exposure. Phyllosilicate crystallization pathways are highly sensitive to the cationic environment, with paragonite favored under high Na^+ activity. This cationic compensation influenced pathway raises a question concerning Na^+ transport during extended exposure: is its mobility sustained or restricted as the system evolves? To address this, we modeled the reaction of boehmite with analcime, a Na-bearing phase identified at stage 2, in the presence of aqueous Si at 300 °C (Fig. 4f). Analcime is shown to gradually dissolve over time under given conditions, releasing Na^+ that becomes incorporated into the paragonite structure. While the simulation predicts nearly complete dissolution within a few days, its reactivity appears overestimated, as practical mass transport is limited by partial encapsulation within the solid matrix. As such, analcime dissolution is thermodynamically favored, yet kinetically constrained, thereby extending the system's residence in stage 2 (Fig. 3b, e). Operations at shallow geological depths may further prolong Stage 2 or divert it toward non-target pathways, potentially spanning a substantial portion of the designed service life, where sustained and spatially heterogeneous mass exchange motivates engineered delivery strategies, such as microcapsules or corrosion-triggered carriers to steer reaction pathways toward target equilibrium phases. Field testing under realistic downhole conditions confirms superior long-term performance retention of the $Al(OH)_3$/SiO_2 formulation over OPC after 9-month exposure in the Newberry geothermal well, despite OPC exhibiting higher initial strength at 1 day (Table S8). Collectively, the revealed competition between kinetic constraints and thermodynamic phase stability provides a guiding principle for rational phase selection toward reliable performance in extreme geothermal environments.

Method

Sample preparation

Aluminum hydroxide ($Al(OH)_3$, Sigma-Aldrich), crystalline silica flour (SiO_2, U.S. Silica Corporation), and sodium metasilicate (Na_2SiO_3, PQ Corporation) were used as precursors. Composites were formulated with 20, 40, or 60 wt% SiO_2 (balance $Al(OH)_3$) and 0, 3, 5, or 9 wt% Na_2SiO_3 relative to total solids. All powders were hand-blended and mixed with tap water for 1 min to form a slurry, which was cast into borosilicate glass tubes (18 mm inner diameter, 150 mm length). The tubes were placed in a humidity chamber (99 ± 1% relative humidity, 85 °C, 24 h) to hydrolyze Na_2SiO_3 and initiate precursor dissolution, after which the gels were transferred to stainless-steel autoclaves (Parr Reactor Models 4622/4680) and hydrothermally cured under two protocols: (i) 200 °C for 24 h followed by 300 °C for 1, 7, or 21 days, (ii) direct exposure at 300 °C or 400 °C for 1 or 7 days. For the 400 °C supercritical exposures, samples were pre-treated at 300 °C for 1 day to mitigate rupture disk failure due to accelerated alkaline corrosion in the autoclave. The heating rate was ~115–120 °C h^{-1} and the autoclave pressure during curing was ~24.1 MPa. After curing, samples were cooled to room temperature, demolded, and stored in sealed containers for subsequent characterization.

Water-fillable porosity measurements

The water-fillable porosity for water-saturated samples was computed by $(W_{wet}\text{-}W_{dry})/V_{vs}\times 100\%$, where W_{wet} is the weight of the water-saturated sample, W_{dry} is the weight of the sample dried for at least four days in a vacuum oven at 65 °C until a sample reaches constant weight and V_{vs} is the volume of sample. All porosity values represent averages from three independent measurements per formulation. Error bars indicate standard deviation.

Content courtesy of Springer Nature, terms of use apply. Rights reserved

https://doi.org/10.1038/s41467-026-72831-9

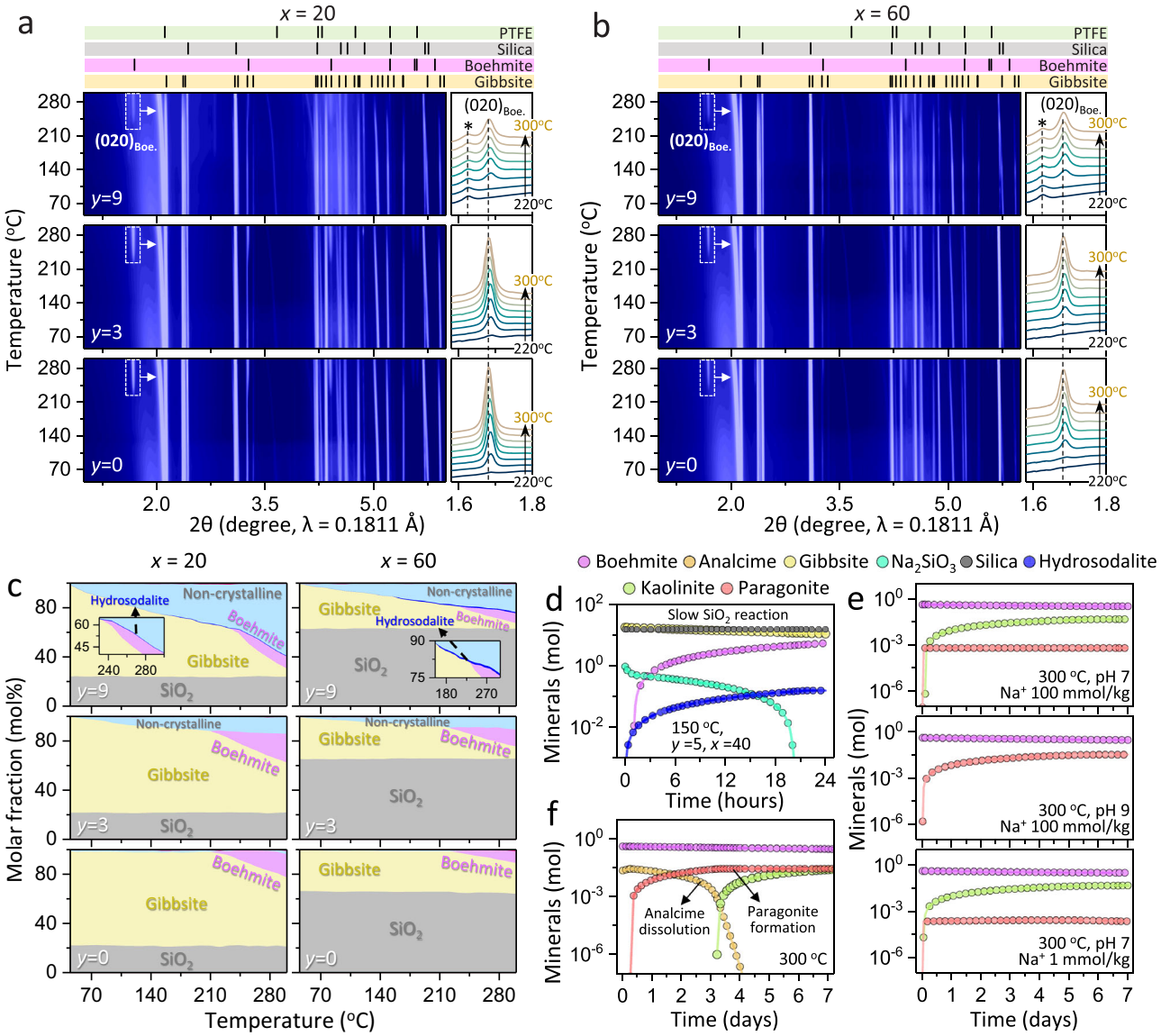


Fig. 4 | Staged phase evolution in aluminosilicate systems. a Contour plots of temperature-resolved X-ray diffraction patterns for formulations with $x = 20$ wt% SiO_2 and varying Na_2SiO_3 activator contents ($y = 0$, 3, 9 wt%), showing the solidification process and phase assemblage. The tick marks correspond to the observed dominant phases: gibbsite, boehmite, silica and polytetrafluoroethylene (PTFE) capillary. A zoomed-in view of the boehmite (020) reflection is shown on the right, tracking its emergence from 220 to 300 °C. The reflection peak of hydrosodalite is marked by the asterisk. **b** Corresponding contour plots for formulations with $x = 60$ wt% SiO_2, highlighting the influence of higher silica content on phase evolution under otherwise identical activator conditions. **c** Evolution of Al and Si distribution among crystalline phases derived from quantitative XRD analysis. The term non-crystalline refers to the decreased Al in crystalline phases, which could be due to the dissolution into the aqueous phase or the formation of amorphous phases. The inset shows the aluminum content in the hydrosodalite phases. **d** Reactivity of coarse-grained crystalline silica under low-temperature and mildly alkaline hydrothermal conditions. Geochemical modeling at 150 °C for 24 h, showing alkali-driven transformation of gibbsite to boehmite, with hydrosodalite derived from dissolved Al and Na_2SiO_3. Silica exhibits limited reactivity under these conditions. **e** Composition-guided selectivity of phyllosilicate crystallization pathways at 300 °C. Geochemical modeling showing composition-dependent transformation of boehmite to phyllosilicates in the presence of aqueous Si, governed by pH and Na^+ concentration. Paragonite formation is allowed only under high alkalinity and Na^+ activity, while kaolinite forms under low pH or limited Na^+ supply. **f** Analcime in the phyllosilicate phase selection. Geochemical modeling showing concurrent formation of kaolinite and paragonite at 300 °C from boehmite and aqueous Si in the presence of analcime, with analcime serving as a high-temperature Na^+ reservoir. Source data are provided as a Source Data file.

In-situ and ex-situ synchrotron XRD measurements

Ex-situ synchrotron XRD patterns were collected at beamline 28-ID-2 (XPD) of the National Synchrotron Light Source II (NSLS-II) at Brookhaven National Laboratory (BNL). The ex-situ samples were crushed into fine powder and mixed uniformly in an acoustic mixer to ensure homogeneity. The wavelength of the X-ray beam for ex-situ sample measurements was 0.1811 Å. The beam size was 0.5 mm (horizontal) × 0.5 mm (vertical). The sodium aluminosilicate phases identified in ex-situ XRD were analyzed using Rietveld refinement of the XRD peaks to determine their chemical formulas, referencing crystallographic databases, including the Crystallography Open Database and the ICDD PDF-5+ database. This approach allowed us to access the Al/Si ratios specific to these structures. Time-resolved in-situ synchrotron XRD patterns were also collected at beamline 28-ID-2 (XPD) under the same X-ray wavelength and beam size as the ex-situ measurements. The gibbsite/silica slurry was mixed with 0, 3 and 9 wt% Na_2SiO_3 activator and encapsulated in a PTFE/quartz in-situ reactor to simulate reactions under hydrothermal conditions uniformly heated using a coil

Content courtesy of Springer Nature, terms of use apply. Rights reserved

heater. The heater temperature was calibrated using a K-type thermocouple. Rietveld refinements of ex-situ XRD patterns were carried out using the TOPAS-Academic V7.12 software. A mask was used to remove the dead pixels and beam-stop shadows. The refined parameters included background coefficients, zero-shift, peak shape parameters, lattice parameters and phase fraction. The atomic XYZ coordinates and isotropic atomic displacement parameters (beq) were fixed to prevent overfitting.

Quantitative analysis of synchrotron in-situ XRD

Rietveld refinements of in-situ synchrotron XRD patterns were performed using TOPAS-Academic V7.12, following a similar refinement protocol as used for ex-situ data except for additional background correction specific to the in-situ reactor. Peaks from an empty PTFE/quartz in-situ reactor were refined using the Le Bail method to extract PTFE lattice parameters and peak intensities at each temperature (see Fig. S20). These parameters were then fixed during the refinement of the sample data at the corresponding temperatures and treated as background. The scale factors obtained from refinement were used to quantify the mass fractions of each crystalline phase, incorporating the relative atomic masses and unit cell volumes. Given the stable synchrotron beam flux, absolute crystalline contents were estimated by normalizing scale factors across phases. Phase fractions were determined using the expression:

$$w_1 = \frac{s_1 m_1 V_1}{\sum_0^i s_i m_i V_i} \quad (1)$$

Where s is the scale factor, m the relative atomic mass, and V the unit cell volume. The Topas command Get (sum_smvs) was used to represent the total crystalline phase. The molar content of Al/Si in each crystalline phase i is calculated using $\mathrm{mol(Al/Si)}_i = s_i V_i n_i$, where n is the number of Al/Si atoms per unit cell. The total crystalline Al/Si content at temperature t_0:

$$\mathrm{mol(Al/Si}, t_0) = \sum_0^i s_i V_i n_i \quad (2)$$

At a given temperature t, the fraction of amorphous Al/Si relative to that at t_0 is given by:

$$\mathrm{mol\%(Amorphous},\ t) = 1 - \frac{\mathrm{mol(Al/Si},\ t)}{\mathrm{mol(Al/Si},\ t_0)} \quad (3)$$

This quantitative analysis enabled the quantification of crystalline phase evolution and the progressive loss of Al/Si species to non-crystalline or dissolved fractions during hydrothermal exposure.

Mechanical testing

Mechanical properties, including compressive strength, Young's modulus, and compressive fracture toughness, were evaluated for cylindrical cement specimens (20 mm diameter × 40 mm height) using an Instron Electromechanical Testing System (Model 5967, 30 kN capacity) operated at a constant displacement rate of 0.5 in/min. Data were recorded at 50 ms intervals, and compression continued until complete mechanical failure. Compressive strength was calculated as the peak load divided by the initial cross-sectional area. Young's modulus was determined as the steepest slope of the initial linear region of the stress–strain curve using a least-squares fit. Compressive fracture toughness was computed as the total area under the stress–strain curve up to failure, normalized by specimen volume. All mechanical values represent averages from three independent measurements per formulation. Error bars indicate standard deviation. Calculations were performed using Bluehill Universal software.

Geochemical modeling

The Geochemist Workbench (GWB, React module) software[74] was used for reaction path modeling to capture the reaction of gibbsite/quartz/Na_2SiO_3 mixture (57/38/5) and the formation of new phases in these experimental systems. Additionally, analcime and boehmite stabilities were assessed in separate reaction path models. The modified version of the thermodynamic database (the Lawrence Livermore National Laboratory thermo.com.V8R6 +) was used, and the database modifications are reported in ref. 37. Reaction path modeling was used to predict solution and solid composition, pH, and mineral saturation as a function of reaction progress and temperature. For the first model that captures the transformation of original gibbsite mixture (57/38/5) (Fig. 4d), the input included all chemical components that were present in the experiments. The tap water composition was provided in Table S7 and compared to the modeling results when de-ionized water was used as the aqueous phase. Swapping de-ionized water with tap water resulted in identical compositions of the primary reaction products, while for the tap water system a few other minerals were predicted in amounts below 1×10^{-7} moles (below the detection limit for XRD, see Fig. S21). The additional ions in the tap water did not change the primary reaction products because their amounts are insignificant given the large solid/liquid ratio in the reactors.

For the prediction of phyllosilicate formation from boehmite shown in Fig. 4e, three test cases were constructed with varying Na^+ concentrations (1 mmol/kg and 100 mmol/kg, charge balanced by Cl^-) and pH (7, 9) values. The basis set of the react file was modified to change the concentrations of Na^+ and pH in these test cases, while keeping the reactant constant: 25 g of boehmite in 1 L of aqueous solution containing 100 mmol/kg of SiO_2(aq). Lastly, analcime stability shown in Fig. 4f was modeled for the aqueous system containing 100 mmol/kg of SiO_2(aq), 100 mmol/kg of Na^+, 200 mmol/kg Cl^- at pH 8. The reactants in this system included 25 g of boehmite and 5 g of analcime. Because thermodynamic data above 300 °C are not available, this was the highest temperature examined in our geochemical models. Kinetic rate parameters were specified for mineral dissolution, while secondary minerals were allowed to precipitate instantaneously. The kinetic dissolution constants were set at 1.0×10^{-12} mol cm^{-2} s^{-1} for gibbsite[75], at 1.0×10^{-8} mol cm^{-2} s^{-1} for SMS, 1.0×10^{-18} mol cm^{-2} s^{-1} for crystalline SiO_2 (quartz), at 1.0×10^{-9} mol cm^{-2} s^{-1} for boehmite, and at 1.0×10^{-8} mol cm^{-2} s^{-1} for analcime. The solid-to-liquid ratio in the mixture transformation models was matched to that of the experiment (44 g of H_2O per 100 g of precursor solid mixture). The solid-to-liquid models in boehmite and analcime stability models were 1000 g of H_2O per 25–30 g of solid. The mineral reactive surface area was set at 10 m^2 g^{-1} for gibbsite and SMS, and at 0.1 m^2 g^{-1} for quartz, 0.001 m^2 g^{-1} for boehmite, and 0.01 m^2 g^{-1} for analcime. The solid phases that were not observed in our experiments (e.g., diaspore and corundum) were suppressed in the models. GWB Act2 module was used to produce the stability diagram for boehmite, kaolinite, and paragonite phases, whose stability is dictated by the activity of Na^+, pH, and dissolved silica SiO_2(aq).

Data availability

Source data are provided with this paper. The minimum dataset necessary to interpret, verify, and extend the findings of this study is provided in the Source Data file. All the raw data relevant to the study are available from the corresponding authors upon request. Source data are provided with this paper.

References

1. Szinai, J. K. et al. Climate change and its influence on water systems increases the cost of electricity system decarbonization. *Nat. Commun.* **15**, 10050 (2024).
2. Peplow, M. How the US tech industry is shaping the transition to green energy. *Nature* **639**, S18–S21 (2025).

Content courtesy of Springer Nature, terms of use apply. Rights reserved

3. Fridleifsson, G. O. & Elders, W. A. The Iceland Deep Drilling Project: a search for deep unconventional geothermal resources. *Geothermics* **34**, 269–285 (2005).
4. Galeczka, I. M. et al. A pre-injection assessment of CO_2 and H_2S mineralization reactions at the Nesjavellir (Iceland) geothermal storage site. *Int. J. Greenh. Gas. Control* **115**, 103610 (2022).
5. Gunnarsson, I. et al. Geothermal gas emission from Hellisheiði and Nesjavellir power plants, Iceland. *GRC Trans.* **37**, 785-789 (2013).
6. Karingithi, C. W., Arnórsson, S. & Grönvold, K. Processes controlling aquifer fluid compositions in the Olkaria geothermal system, Kenya. *J. Volcanol. Geotherm. Res.* **196**, 57–76 (2010).
7. Huet, B. M., Prevost, J. H. & Scherer, G. W. Quantitative reactive transport modeling of Portland cement in CO2-saturated water. *Int. J. Greenh. Gas. Control* **4**, 561–574 (2010).
8. Glosser, D., Isgor, O. B. & Weiss, W. J. Non-equilibrium thermodynamic modeling framework for ordinary Portland cement/supplementary cementitious material systems. *ACI Mater. J.* **117**, 111–123 (2020).
9. Glosser, D., Suraneni, P., Isgor, O. B. & Weiss, W. J. Estimating reaction kinetics of cementitious pastes containing fly ash. *Cem. Concr. Compos.* **112**, 103655 (2020).
10. Palou, M. T., Kuzielová, E., Žemlička, M., Tkácz, J. & Másilko, J. Insights into the hydration of Portland cement under hydrothermal curing. *J. Therm. Anal. Calorim.* **138**, 4155–4165 (2019).
11. Ostwald, W. Studien uber die Bildung und Umwandlung fester Korper. *Z. Phys. Chem.* **22**, 289–330 (1897).
12. Provis, J. L. Alkali-activated materials. *Cem. Concr. Res.* **114**, 40–48 (2018).
13. Liu, Y., Hu, X., Du, Y., Nematollahi, B. & Shi, C. A review on high-temperature resistance of geopolymer concrete. *J. Build. Eng.* **98**, 111241 (2024).
14. Zhang, H. Y., Kodur, V., Wu, B., Cao, L. & Wang, F. Thermal behavior and mechanical properties of geopolymer mortar after exposure to elevated temperatures. *Constr. Build. Mater.* **109**, 17–24 (2016).
15. Alonso, C. & Fernandez, L. Dehydration and rehydration processes of cement paste exposed to high temperature environments. *J. Mater. Sci.* **39**, 3015–3024 (2004).
16. Pei, Y., Agostini, F. & Skoczylas, F. The effects of high temperature heating on the gas permeability and porosity of a cementitious material. *Cem. Concr. Res.* **95**, 141–151 (2017).
17. Rickard, W. D. A., Kealley, C. S. & van Riessen, A. Thermally induced microstructural changes in fly ash geopolymers: experimental results and proposed model. *J. Am. Ceram. Soc.* **98**, 929–939 (2015).
18. Taylor, H. F. *Cement chemistry* (Thomas Telford London, 1997).
19. Welch, J. H. & Gutt, W. Tricalcium silicate and its stability within the system CaO-SiO_2. *J. Am. Ceram. Soc.* **42**, 11–15 (1959).
20. Yuan, G. et al. A review of feldspar alteration and its geological significance in sedimentary basins: From shallow aquifers to deep hydrocarbon reservoirs. *Earth Sci. Rev.* **191**, 114–140 (2019).
21. Cong, P. & Cheng, Y. Advances in geopolymer materials: a comprehensive review. *J. Traffic Transp. Eng.* **8**, 283–314 (2021).
22. Singh, B., Ishwarya, G., Gupta, M. & Bhattacharyya, S. K. Geopolymer concrete: a review of some recent developments. *Constr. Build. Mater.* **85**, 78–90 (2015).
23. Barbosa, V. F. F. & MacKenzie, K. J. D. Thermal behaviour of inorganic geopolymers and composites derived from sodium polysialate. *Mater. Res. Bull.* **38**, 319–331 (2003).
24. Barbosa, V. F. F. & MacKenzie, K. J. D. Synthesis and thermal behaviour of potassium sialate geopolymers. *Mater. Lett.* **57**, 1477–1482 (2003).
25. Rashad, A. M. & Ouda, A. S. An investigation on alkali-activated fly ash pastes modified with quartz powder subjected to elevated temperatures. *Constr. Build. Mater.* **122**, 417–425 (2016).
26. Rashad, A. M., Hassan, A. A. & Zeedan, S. R. An investigation on alkali-activated Egyptian metakaolin pastes blended with quartz powder subjected to elevated temperatures. *Appl. Clay Sci.* **132-133**, 366–376 (2016).
27. Aydın, S. & Baradan, B. Effect of pumice and fly ash incorporation on high temperature resistance of cement based mortars. *Cem. Concr. Res.* **37**, 988–995 (2007).
28. Kong, D. L. Y. & Sanjayan, J. G. Effect of elevated temperatures on geopolymer paste, mortar and concrete. *Cem. Concr. Res.* **40**, 334–339 (2010).
29. Valencia Saavedra, W. G. & Mejía de Gutiérrez, R. Performance of geopolymer concrete composed of fly ash after exposure to elevated temperatures. *Constr. Build. Mater.* **154**, 229–235 (2017).
30. Masi, G., Rickard, W. D. A., Bignozzi, M. C. & van Riessen, A. The effect of organic and inorganic fibres on the mechanical and thermal properties of aluminate activated geopolymers. *Compos. Part B: Eng.* **76**, 218–228 (2015).
31. Pham, K. V. A., Nguyen, K. T., Le, T. A. & Lee, K. Investigation of impact behavior of innovative non-curing steel fiber geopolymer composites. *Case Stud. Constr. Mater.* **16**, e01011 (2022).
32. Poon, C. S., Shui, Z. H. & Lam, L. Compressive behavior of fiber reinforced high-performance concrete subjected to elevated temperatures. *Cem. Concr. Res.* **34**, 2215–2222 (2004).
33. Snellings, R. et al. Hydration kinetics of ternary slag-limestone cements: Impact of water to binder ratio and curing temperature. *Cem. Concr. Res.* **151**, 106647 (2022).
34. Yu, J., Li, G. & Leung, C. K. Y. Hydration and physical characteristics of ultrahigh-volume fly ash-cement systems with low water/binder ratio. *Constr. Build. Mater.* **161**, 509–518 (2018).
35. Chan, Y. N., Peng, G. F. & Anson, M. Residual strength and pore structure of high-strength concrete and normal strength concrete after exposure to high temperatures. *Cem. Concr. Compos.* **21**, 23–27 (1999).
36. Kashani, A., Ngo, T. D., Walkley, B. & Mendis, P. Thermal performance of calcium-rich alkali-activated materials: a microstructural and mechanical study. *Constr. Build. Mater.* **153**, 225–237 (2017).
37. Liu, S. et al. Geo-responsive chemomechanics in aluminum oxyhydroxide via alkali-driven dehydroxylation for supercritical geothermal systems. *ACS Mater. Lett.* **7**, 1869–1878 (2025).
38. Belviso, C., Lettino, A. & Cavalcante, F. Influence of synthesis method on LTA time-dependent stability. *Molecules* **23**, 2122 (2018).
39. Johnson, G. K., Flotow, H. E. & O'Hare, P. A. G. Thermodynamic studies of zeolites: analcime and dehydrated analcime. *Am. Mineral.* **67**, 736–748 (1982).
40. Cruciani, G. Zeolites upon heating: factors governing their thermal stability and structural changes. *J. Phys. Chem. Solids* **67**, 1973–1994 (2006).
41. Henderson, C. M. B. Feldspathoid Stabilities and Phase Inversions — A Review. in *Feldspars and Feldspathoids: Structures, Properties and Occurrences* (ed. Brown, W. L.) 471-499 (Springer Netherlands, 1984).
42. Gualtieri, A. F. & Aprea, P. The structure of K-hydrosodalite. *Microporous Mesoporous Mater.* **96**, 276–286 (2006).
43. Hassan, I., Antao, S. M. & Parise, J. B. Cancrinite: crystal structure, phase transitions, and dehydration behavior with temperature. *Am. Mineral.* **91**, 1117–1124 (2006).
44. Smith, J. V. Critical review of synthesis and occurrence of plagioclase feldspars and a possible phase diagram. *J. Geol.* **80**, 505–525 (1972).
45. Ribbe, P. H. *Feldspar mineralogy* (Walter de Gruyter GmbH & Co KG, 2018).
46. El-Shazly, A. E.-D. K. On the thermodynamic data of kaolinite. *Am. Mineral.* **80**, 1048–1053 (1995).

Content courtesy of Springer Nature, terms of use apply. Rights reserved

47. Kubliha, M. et al. Comparison of dehydration in kaolin and illite using DC conductivity measurements. *Appl. Clay Sci.* **149**, 8–12 (2017).
48. Comodi, P. & Zanazzi, P. F. Structural thermal behavior of paragonite and its dehydroxylate: a high-temperature single-crystal study. *Phys. Chem. Miner.* **27**, 377–385 (2000).
49. Li, G. et al. Thermal transformation of pyrophyllite and alkali dissolution behavior of silicon. *Appl. Clay Sci.* **99**, 282–288 (2014).
50. Brindley, G. W. & Nakahira, M. The Kaolinite-Mullite reaction series: II, Metakaolin. *J. Am. Ceram. Soc.* **42**, 314–318 (1959).
51. Kim, G. et al. Evaluation of the thermal stability of metakaolin-based geopolymers according to Si/Al ratio and sodium activator. *Cem. Concr. Compos.* **150**, 105562 (2024).
52. Sivasakthi, M., Jeyalakshmi, R., Rajamane, N. P. & Jose, R. Thermal and structural micro analysis of micro silica blended fly ash based geopolymer composites. *J. Non-Cryst. Solids* **499**, 117–130 (2018).
53. Thokchom, S., Mandal, K. K. & Ghosh, S. Effect of Si/Al ratio on performance of fly ash geopolymers at elevated temperature. *Arab. J. Sci. Eng.* **37**, 977–989 (2012).
54. Liu, C., Ma, H., Qiu, Y. & Gao, Y. Ion distribution in analcime-leucite mineral and Na+-K+ mixed solution. *Ceram. Int.* **45**, 15566–15570 (2019).
55. Walton, R. I. et al. An in situ energy-dispersive X-ray diffraction study of the hydrothermal crystallization of Zeolite A. 1. Influence of reaction conditions and transformation into sodalite. *J. Phys. Chem. B* **105**, 83–90 (2001).
56. Novembre, D., Gimeno, D. & Del Vecchio, A. Synthesis and characterization of Na-P1 (GIS) zeolite using a kaolinitic rock. *Sci. Rep.* **11**, 4872 (2021).
57. Cheng, H., Liu, Q., Yang, J., Ma, S. & Frost, R. L. The thermal behavior of kaolinite intercalation complexes-A review. *Thermochim. Acta* **545**, 1–13 (2012).
58. Khajavi, S., Sartipi, S., Gascon, J., Jansen, J. C. & Kapteijn, F. Thermostability of hydroxy sodalite in view of membrane applications. *Microporous Mesoporous Mater.* **132**, 510–517 (2010).
59. Król, M. K. & Jeleń, P. The effect of heat treatment on the structure of zeolite A. *Materials* **14**, 4642 (2021).
60. Huo, Z. et al. Thermal study of NaP zeolite with different morphologies. *J. Therm. Anal. Calorim.* **111**, 365–369 (2013).
61. Kim, H. N. & Lee, S. K. Temperature-induced amorphization of Na-zeolite A: a view from multi-nuclear high-resolution solid-state NMR. *Am. Mineral.* **99**, 1996–2007 (2014).
62. Al-mashhadani, M. M., Canpolat, O., Aygörmez, Y., Uysal, M. & Erdem, S. Mechanical and microstructural characterization of fiber reinforced fly ash based geopolymer composites. *Constr. Build. Mater.* **167**, 505–513 (2018).
63. Aiken, T. A., Kwasny, J., Sha, W. & Soutsos, M. N. Effect of slag content and activator dosage on the resistance of fly ash geopolymer binders to sulfuric acid attack. *Cem. Concr. Res.* **111**, 23–40 (2018).
64. Aliques-Granero, J., Tognonvi, M. T. & Tagnit-Hamou, A. Durability study of AAMs: sulfate attack resistance. *Constr. Build. Mater.* **229**, 117100 (2019).
65. Alrefaei, Y., Wang, Y.-S. & Dai, J.-G. The effectiveness of different superplasticizers in ambient cured one-part alkali activated pastes. *Cem. Concr. Compos.* **97**, 166–174 (2019).
66. Ascensão, G., Seabra, M. P., Aguiar, J. B. & Labrincha, J. A. Red mud-based geopolymers with tailored alkali diffusion properties and pH buffering ability. *J. Clean. Prod.* **148**, 23–30 (2017).
67. Isa, M. N. & Awang, H. Characteristics of palm oil fuel ash geopolymer mortar activated with wood ash lye cured at ambient temperature. *J. Build. Eng.* **66**, 105851 (2023).
68. Fu, Q. et al. Coupled alkali-feldspar dissolution and secondary mineral precipitation in batch systems: 1. New experiments at 200 °C and 300 bars. *Chem. Geol.* **258**, 125–135 (2009).
69. Bjørlykke, K. & Aagaard, P. Clay minerals in North Sea sandstones. in *Origin, Diagenesis, and Petrophysics of Clay Minerals in Sandstones*, Vol. 47 (eds. Houseknecht, D. W. & Pittman, E. D.) (SEPM Society for Sedimentary Geology, 1992).
70. Yang, Y. et al. Engineering flexible superblack materials. *Nat. Commun.* **16**, 4650 (2025).
71. Rufer, S., Nitzsche, M. P., Garimella, S., Lake, J. R. & Varanasi, K. K. Hierarchically conductive electrodes unlock stable and scalable CO_2 electrolysis. *Nat. Commun.* **15**, 9429 (2024).
72. Steele, J. A. et al. An embedded interfacial network stabilizes inorganic CsPbI3 perovskite thin films. *Nat. Commun.* **13**, 7513 (2022).
73. Ashammakhi, N. et al. Biodegradable implantable sensors: materials design, fabrication, and applications. *Adv. Funct. Mater.* **31**, 2104149 (2021).
74. Bethke, C. M. *Geochemical and biogeochemical reaction modeling* (Cambridge University Press, 2022).
75. Nagy, K. L. & Lasaga, A. C. Dissolution and precipitation kinetics of gibbsite at 80°C and pH 3: The dependence on solution saturation state. *Geochim. et. Cosmochim. Acta* **56**, 3093–3111 (1992).

Acknowledgements

We thank Yusuf Celebi and John Trunk for technical support. We thank Michelle Devoe for assistance with sample preparation and synchrotron beamline measurements. We also thank Gwen Wright for assistance with SEM and Kim Kisslinger for assistance with sample preparation. T.P., S.L., J.B., and T.S. disclose support for the research of this work from the U.S. Department of Energy, Office of Science Energy Earthshot Initiative, as part of the Center for Coupled Chemo-Mechanics of Cementitious Composites for EGS (C4M) project at Brookhaven National Laboratory under Contract No. 2026-BNL-IS012-FUND. A.G.I. discloses support for the research of this work from the Center for Coupled Chemo-Mechanics of Cementitious Composites for EGS (C4M) project at Sandia National Laboratories under Contract No. FWP 24-026492. T.P. and T.S. disclose partial support for the research of this work from the Geothermica project Sustainable Geothermal Well Cements for Challenging Thermo-Mechanical Conditions (TEST-CEM), No. 2003184001. The project has been subsidized through the Cofund GEOTHERMICA by DOE (the USA), RVO NL (the Netherlands), and the Research Council of Norway. This research used 28-ID-2 (XPD) and 27-ID (HEX) beamlines at the National Synchrotron Light Source II, a U.S. DOE Office of Science User Facility operated for the DOE Office of Science by Brookhaven National Laboratory under Contract No. DE-SC0012704. This research also used the Center for Functional Nanomaterials (CFN), which is supported by the U.S. Department of Energy, Office of Basic Energy Sciences, under Contract No. DE-AC02-98CH10886. This article was authored in part by an employee of National Technology & Engineering Solutions of Sandia, LLC under Contract No. DE-NA0003525 with the U.S. Department of Energy.

Author contributions

T.P. and T.S. conceived this work; T.P. and T.S. carried out sample preparations and mechanical testing. S.L. and T.S. analyzed the results of mechanical testing. S.L., M.T., and J.B. performed ex-situ synchrotron XRD measurements; S.L. and J.B. conducted Rietveld refinement of the ex-situ data. S.L. and J.B. performed the in-situ synchrotron XRD measurements. S.L. and J.B. conducted quantitative XRD analysis. S.L. and M.D. conducted the synchrotron X-ray tomography measurements. S.L. and T.P. contributed to the interpretation of materials design. A.G.I. conducted geochemical modeling. S.L. wrote the manuscript with critical input from all other authors. All authors edited and approved the manuscript.

Competing interests

The authors declare no competing interests.

Content courtesy of Springer Nature, terms of use apply. Rights reserved

Additional information

Supplementary information The online version contains supplementary material available at https://doi.org/10.1038/s41467-026-72831-9.

Correspondence and requests for materials should be addressed to Sizhan Liu, Jianming Bai, Anastasia G. Ilgen or Tatiana Pyatina.

Peer review information *Nature Communications* thanks the anonymous reviewers for their contribution to the peer review of this work. A peer review file is available.

Reprints and permissions information is available at http://www.nature.com/reprints

Publisher's note Springer Nature remains neutral with regard to jurisdictional claims in published maps and institutional affiliations.

Open Access This article is licensed under a Creative Commons Attribution-NonCommercial-NoDerivatives 4.0 International License, which permits any non-commercial use, sharing, distribution and reproduction in any medium or format, as long as you give appropriate credit to the original author(s) and the source, provide a link to the Creative Commons licence, and indicate if you modified the licensed material. You do not have permission under this licence to share adapted material derived from this article or parts of it. The images or other third party material in this article are included in the article's Creative Commons licence, unless indicated otherwise in a credit line to the material. If material is not included in the article's Creative Commons licence and your intended use is not permitted by statutory regulation or exceeds the permitted use, you will need to obtain permission directly from the copyright holder. To view a copy of this licence, visit http://creativecommons.org/licenses/by-nc-nd/4.0/.

© The Author(s) 2026

Content courtesy of Springer Nature, terms of use apply. Rights reserved

Terms and Conditions

Springer Nature journal content, brought to you courtesy of Springer Nature Customer Service Center GmbH ("Springer Nature").
Springer Nature supports a reasonable amount of sharing of research papers by authors, subscribers and authorised users ("Users"), for small-scale personal, non-commercial use provided that all copyright, trade and service marks and other proprietary notices are maintained. By accessing, sharing, receiving or otherwise using the Springer Nature journal content you agree to these terms of use ("Terms"). For these purposes, Springer Nature considers academic use (by researchers and students) to be non-commercial.
These Terms are supplementary and will apply in addition to any applicable website terms and conditions, a relevant site licence or a personal subscription. These Terms will prevail over any conflict or ambiguity with regards to the relevant terms, a site licence or a personal subscription (to the extent of the conflict or ambiguity only). For Creative Commons-licensed articles, the terms of the Creative Commons license used will apply.
We collect and use personal data to provide access to the Springer Nature journal content. We may also use these personal data internally within ResearchGate and Springer Nature and as agreed share it, in an anonymised way, for purposes of tracking, analysis and reporting. We will not otherwise disclose your personal data outside the ResearchGate or the Springer Nature group of companies unless we have your permission as detailed in the Privacy Policy.
While Users may use the Springer Nature journal content for small scale, personal non-commercial use, it is important to note that Users may not:

1. use such content for the purpose of providing other users with access on a regular or large scale basis or as a means to circumvent access control;
2. use such content where to do so would be considered a criminal or statutory offence in any jurisdiction, or gives rise to civil liability, or is otherwise unlawful;
3. falsely or misleadingly imply or suggest endorsement, approval , sponsorship, or association unless explicitly agreed to by Springer Nature in writing;
4. use bots or other automated methods to access the content or redirect messages
5. override any security feature or exclusionary protocol; or
6. share the content in order to create substitute for Springer Nature products or services or a systematic database of Springer Nature journal content.

In line with the restriction against commercial use, Springer Nature does not permit the creation of a product or service that creates revenue, royalties, rent or income from our content or its inclusion as part of a paid for service or for other commercial gain. Springer Nature journal content cannot be used for inter-library loans and librarians may not upload Springer Nature journal content on a large scale into their, or any other, institutional repository.
These terms of use are reviewed regularly and may be amended at any time. Springer Nature is not obligated to publish any information or content on this website and may remove it or features or functionality at our sole discretion, at any time with or without notice. Springer Nature may revoke this licence to you at any time and remove access to any copies of the Springer Nature journal content which have been saved.
To the fullest extent permitted by law, Springer Nature makes no warranties, representations or guarantees to Users, either express or implied with respect to the Springer nature journal content and all parties disclaim and waive any implied warranties or warranties imposed by law, including merchantability or fitness for any particular purpose.
Please note that these rights do not automatically extend to content, data or other material published by Springer Nature that may be licensed from third parties.
If you would like to use or distribute our Springer Nature journal content to a wider audience or on a regular basis or in any other manner not expressly permitted by these Terms, please contact Springer Nature at

onlineservice@springernature.com